Editors' Suggestion

# Experimental verification of the reflection matrix description in linear magneto-optics

Carmen Martín Valderrama, Mikel Quintana, and Andreas Berger*
*CIC nanoGUNE BRTA, E-20018 Donostia-San Sebastián, Spain*

(Received 10 February 2023; accepted 22 June 2023; published 12 July 2023)

We have experimentally studied the accuracy of the Jones-type reflection matrix **R** that describes light reflection from a magnetic sample exhibiting the magneto-optical (MO) Kerr effect (MOKE). For this purpose, we performed a comprehensive experimental study, utilizing generalized MO ellipsometry, which allows for the simultaneous measurement of all complex-valued elements of **R** for arbitrary magnetization vector orientations. For the collection of suitable datasets under appropriate test conditions, we also fabricated and utilized a thin film sample that exhibits a uniform magnetization state, whose vector orientation can be easily rotated by an applied magnetic field. This approach enabled us to systematically and simultaneously vary the MOKE coefficients of **R**, which permitted us to verify the accuracy of **R** with high precision. While we observe the widely used standard formulation of **R** to be correct under most experimental conditions, we also found small systematic deviations for some specific cases. However, these deviations are not indicative of a limited correctness of **R**, but instead, they are related to the material assumptions that are commonly made for the derivation of **R**. For our specific sample here, the origin of the deviation is MO anisotropy, and upon considering this material property accurately, an exact description of all experimental results by **R** can be reestablished.

DOI: 10.1103/PhysRevB.108.014415

## I. INTRODUCTION

The magneto-optical (MO) Kerr effect (MOKE) was first documented by John Kerr [1–3] when he observed a change in the polarization state of light reflected from a magnetic piece of iron. Since then, MOKE has found widespread applications in areas such as magnetic domain observation via Kerr microscopy [4–8], materials characterization through MOKE spectroscopy methods [9], and the observation of ultrafast magnetization dynamics [7,10], among others [11]. Moreover, MOKE is nowadays widely used as a powerful, contactless, and nondestructive measurement technique to study electronic and magnetic properties in magnetic materials and devices [3,5,9]. It is frequently utilized to monitor magnetization reversal [8,12–15], including magnetization vector information [16,17], which has also been achieved in time-resolved studies on the ultrafast time scale [18–20]. Even extremely small magnetic signals can be efficiently detected using MOKE techniques [21,22], which also led to relevant contributions in plasmonics [23] and spintronics [24,25].

Hereby, it should be noted that MOKE has been used frequently for quantitative magnetometry [16,26,27] and more recently even in vector magnetometry approaches as well [16–20,26,28,29], which is enabled by detecting, quantifying, and separating the MOKE contributions of different magnetization vector components. In most MOKE studies and applications, however, the experimental data are determining only a subset of the overall reflection matrix **R** of the sample under investigation [30–33], which is the key quantity that describes the light reflection process, even if there are some studies, in which the whole reflection matrix is being measured [19,20,30]. The Jones formalism reflection matrix **R** can be derived by solving Maxwell's equations using electromagnetic theory and proper boundary conditions. In the most commonly used case of a bulk sample that is magnetic but otherwise optically isotropic and including only linear MO terms in the materials properties as well as limiting the derivation itself to such linear terms only, **R** is given as [34]

$$\mathbf{R} = r_p\begin{pmatrix} \tilde{r}_s & \tilde{\alpha}+\tilde{\gamma} \\ -\tilde{\alpha}+\tilde{\gamma} & 1+\tilde{\beta} \end{pmatrix} = r_p\begin{pmatrix} \tilde{r}_s & \tilde{\alpha}_0\cdot m_x+\tilde{\gamma}_0\cdot m_z \\ -\tilde{\alpha}_0\cdot m_x+\tilde{\gamma}_0\cdot m_z & 1+\tilde{\beta}_0\cdot m_y \end{pmatrix}, \quad (1)$$

with $m_{x,y,z}$ being the normalized magnetization components in Cartesian coordinates, defined relative to the sample surface and the plane of incidence, as shown in the schematics of Fig. 1. Hereby, $r_s$ and $r_p$ are the conventional Fresnel coefficients (with $\tilde{r}_s = r_s/r_p$) and $\tilde{\alpha}$, $\tilde{\beta}$, and $\tilde{\gamma}$ are the MOKE coefficients associated with each of the normalized magnetization components $m_x$, $m_y$, and $m_z$ divided by $r_p$, respectively. Given the abovementioned linear MO assumption, the $\tilde{\alpha}$, $\tilde{\beta}$, and $\tilde{\gamma}$ MOKE coefficients are linearly dependent on the corresponding normalized magnetization vector component, as represented in Eq. (1). All optical and MO coefficients in Eq. (1) are complex parameters that depend on the wavelength of the light as well as the angle of incidence. Also, it ought to be mentioned that, for virtually all materials and optical configurations $\tilde{\alpha}$, $\tilde{\beta}$, and $\tilde{\gamma}$ are far smaller than the purely optical elements of **R**. Furthermore, the same fundamental form of the reflection matrix, shown in Eq. (1) is derived for a

*a.berger@nanogune.eu

 

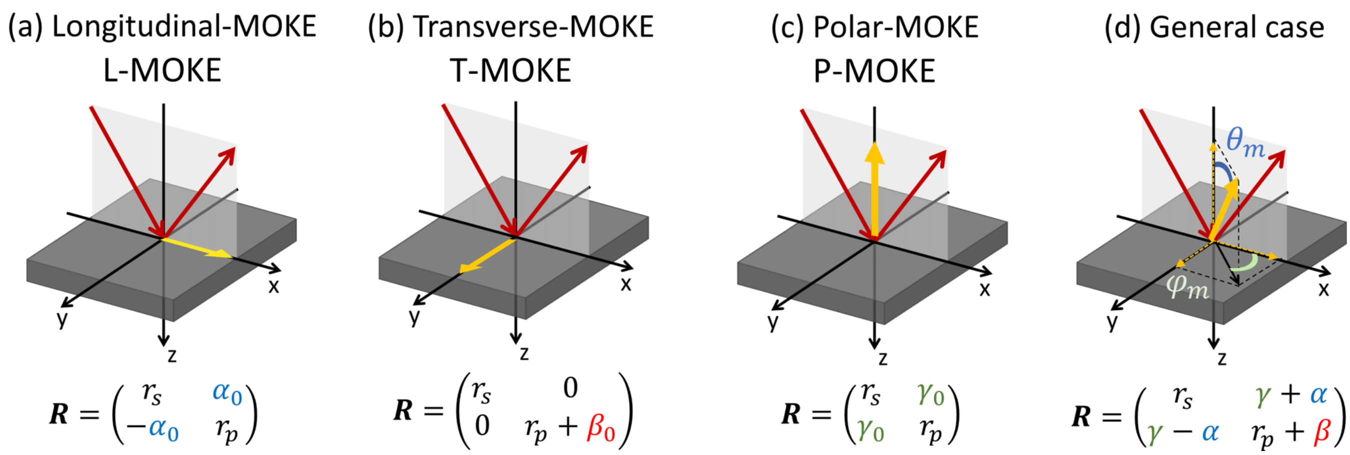


FIG. 1. Geometrical schematic of (a) longitudinal (L-), (b) transverse (T-), and (c) polar magneto-optical Kerr effect (P-MOKE); (d) represents the most general case of exhibiting a linear superposition of L-, T-, and P-MOKE simultaneously. The normalized magnetization vector $\vec{m}$ is represented by the yellow arrow, and its orientation is defined by angles $\theta_m$ and $\varphi_m$. The corresponding reflection matrices are shown below each subfigure. The path of the light beam is represented by the red arrow, and it defines the plane of incidence, represented by a light gray plane.

multitude of different material systems, including optically thick magnetic films as well as for ultrathin magnetic films, with or without nonmagnetic overcoats [34–38], making Eq. (1) a crucially relevant equation for quantitative MOKE observations for all kinds of sample types.

The conventional MOKE classification scheme is also represented in the schematics of Fig. 1. The longitudinal MOKE (L-MOKE) and transverse MOKE (T-MOKE) are the effects generated by an in-plane magnetization parallel to the plane of incidence or perpendicular to it, as we can see in Figs. 1(a) and 1(b), respectively. The polar MOKE (P-MOKE) appears when having an out-of-plane magnetization component, as represented in Fig. 1(c). Below the three schemes represented in Figs. 1(a)–1(c), the corresponding reflection matrices as defined by Eq. (1) are shown. Figure 1(d) represents the most general case, in which all three magnetization components appear, and therefore, the reflection matrix includes all three MO parameters as a linear superposition of the individual MO terms.

As already mentioned, Eq. (1) is the result of rigorous albeit approximate theoretical derivations for numerous sample geometries, and for a long time, no deviations from it were reported, even if a rigorous experimental verification has not been conducted either. More recently, however, there have been reports of linear MOKE effects that appear to be independent or partially independent from the magnetization of the sample [39–41], and deviations from **R** were observed that have been associated with depth-modulated magnetic states [21]. Thus, it is crucially important to experimentally verify the correctness of the above **R** expression in Eq. (1), at least for conventional ferromagnetic materials or films, and to do so in a quantitatively precise way, which is the core objective of this paper. As such, this paper does not simply fill an overlooked experimental gap, but it also opens broad possibilities because a verification that **R** indeed describes MO effects of a film in a quantitatively accurate manner enables the experimental utilization of deviations from **R** to extract additional and relevant sample information. For instance, we demonstrated recently that a magnetic-state-induced phase change of the transverse MOKE coefficient $\tilde{\beta}$ in a bilayer magnetic system is associated with the nonsynchronous magnetic response of the constituting magnetic layers [21]. However, this interpretation is only correct and meaningful if the conventional reflection matrix **R** description for a single magnetic film in Eq. (1) is confirmed by comprehensive and precise experiments, which is exactly the purpose of this paper. Thus, the accurate and precise verification of Eq. (1) for single magnetic films is crucially necessary to facilitate the utilization of experimental deviations from **R** in more complex magnetic sample structures for the purpose of developing and advancing MOKE characterization techniques.

To enable such a quantitative analysis of MOKE in a magnetic film sample, it is important to control the Cartesian components of the magnetization, given that they define the individual elements in **R** according to Eq. (1). This can be achieved by utilizing a magnetic sample that exhibits a uniform magnetization state for any applied field value and orientation so that the absolute value of the magnetization vector remains constant upon rotation. In this way, different magnetization components are correlated and can be quantitatively compared with each other by means of the normalized magnetization vector $\vec{m} = \vec{M}/M_s$ with $|\vec{m}| = 1$ and $m_x = \sin(\theta_m)\cos(\varphi_m)$, $m_y = \sin(\theta_m)\sin(\varphi_m)$, and $m_z = \cos(\theta_m)$, with $\varphi_m$ and $\theta_m$ being the polar coordinates of the magnetization vector as represented in Fig. 1(d) and with $M_s$ being the saturation magnetization. The three Cartesian magnetization components are fully correlated, which according to Eq. (1), correlates the MOKE parameters of **R**. Given this MOKE correlation, one can derive relevant test conditions that should be satisfied if Eq. (1) is indeed correct.

For the case of a purely in-plane magnetization vector, there is no P-MOKE, and the correlation between the Cartesian magnetization components is $m_x^2 + m_y^2 = 1$. Therefore, given the fact that the complex parameters $\tilde{\alpha}$ and $\tilde{\beta}$ depend linearly on $m_x$ and $m_y$ in Eq. (1), with $\tilde{\alpha}_0$ and $\tilde{\beta}_0$ being the corresponding coefficients, one can show that the absolute values of $\tilde{\alpha}$ and $\tilde{\beta}$ are correlated via

$$\left(\frac{|\tilde{\alpha}|}{|\tilde{\alpha}_0|}\right)^2 + \left(\frac{|\tilde{\beta}|}{|\tilde{\beta}_0|}\right)^2 = 1, \tag{2}$$

which describes an ellipse equation. The corresponding phases of the complex parameters $\tilde{\alpha}$ and $\tilde{\beta}$ are concurrently expected to remain constant for any in-plane magnetization state, i.e.,

$$\phi_{\tilde{\alpha}} = \phi_{\tilde{\alpha}_0}, \ \ \phi_{\tilde{\beta}} = \phi_{\tilde{\beta}_0}. \tag{3}$$

For the general case in which the magnetization vector also has an out-of-plane component, the magnetization component correlation is $m_x^2 + m_y^2 + m_z^2 = 1$, and the MOKE parameters can be shown to fulfill

$$\left(\frac{|\tilde{\alpha}|}{|\tilde{\alpha}_0|}\right)^2 + \left(\frac{|\tilde{\beta}|}{|\tilde{\beta}_0|}\right)^2 + \left(\frac{|\tilde{\gamma}|}{|\tilde{\gamma}_0|}\right)^2 = 1, \tag{4}$$

which describes an ellipsoid equation, while at the same time, the phases of $\tilde{\alpha}$, $\tilde{\beta}$, and $\tilde{\gamma}$ are expected to remain constant, independent of the magnetization orientation, i.e.,

$$\phi_{\tilde{\alpha}} = \phi_{\tilde{\alpha}_0}, \ \ \phi_{\tilde{\beta}} = \phi_{\tilde{\beta}_0}, \ \ \phi_{\tilde{\gamma}} = \phi_{\tilde{\gamma}_0}. \tag{5}$$

An additional condition of the accuracy of Eq. (1) for any type of magnetization orientation is the fact that the matrix elements that are not explicitly magnetization dependent are purely optical, and thus, $\mathrm{Re}(\tilde{r}_s)$ and $\mathrm{Im}(\tilde{r}_s)$ should remain constant for any magnetization state if Eq. (1) is indeed correct.

To experimentally achieve meaningful test conditions and verify the relations derived above, and in doing so verify the accuracy of Eq. (1), the following conditions need to be fulfilled: we need to (i) fabricate a sample that enables us to access a broad range of magnetization orientations in the same MO measurement geometry while keeping the absolute magnetization value constant and (ii) utilize an experimental methodology that allows us to measure the full reflection matrix for all magnetization orientations. To achieve (i), we conceived a specific sample design, fabricated a corresponding sample, and for our MOKE measurements, we utilized generalized magneto-optical ellipsometry (GME), which allowed us to fulfill condition (ii). These two experimental aspects enabled us to verify that Eqs. (2)–(5) are correct, which in turn confirms the validity of Eq. (1) experimentally in a quantitatively accurate manner. Sample design and fabrication as well as the GME technique are described in Sec. II. Section III contains the obtained experimental results, upon which conclusions are drawn in Sec. IV.

## II. EXPERIMENTAL DETAILS

### A. Sample design and fabrication

To have a sample system whose reflection matrix elements are correlated as described by Eqs. (2)–(5) and thus build a test case for the accuracy of Eq. (1), one needs a material system that is well described by a fixed-length magnetization vector that can rotate as the external magnetic field changes, i.e., a so-called macrospin-type sample. Such a desired sample can be achieved with a thin film sample that exhibits uniaxial anisotropy with an in-plane easy axis (EA) to avoid domain formation and associated deviations from macrospin behavior. In addition, it is important that our sample system has laterally uniform magnetization properties, which will enable a quantitatively accurate interpretation of macroscopic magnetization and MO properties [12,42]. We chose a Co-Pt alloy to carry out this study, as it can fulfill the abovementioned conditions and has sufficiently high and uniform anisotropy [43] so that we can have excellent field control of the magnetization orientation while covering a wide range of rotation states of the magnetization vector. Specifically, we want a Co-Pt layer with hexagonal close-packed crystal structure and $(10\underline{1}0)$ surface orientation because it contains the [0001] direction in the surface plane, which is the EA of magnetization. To fabricate such a layer, we utilize a specific epitaxial growth sequence, which is represented in Fig. 2(a). A hydrofluoric-acid-etched Si (110) substrate is used, followed by 75 nm of Ag (110) and 20 nm of Cr (211) template layers that allow for the high-quality epitaxial growth of Co and Co-alloy $(10\underline{1}0)$ films, as has been demonstrated in several previous studies [12,44–48]. Here, the specific magnetic layer is a 11-nm-thick $Co_{0.95}Pt_{0.05}$ $(10\underline{1}0)$ film, on top of which 2 nm of Cr and a 10-nm $SiO_2$ overcoat are deposited to have the same interface materials on both surfaces of the Co-Pt magnetic layer and to avoid surface oxidation and contaminations of the layers underneath. The layer sequence that forms our sample has been grown by sputter deposition at room temperature in a 3-mTorr pure Ar atmosphere. Its structural properties have been characterized by x-ray diffraction measurements, confirming the epitaxial nature of the sample, which is consistent with the findings of numerous reports for other Co-alloy samples [12,44–48].

To also verify that the epitaxially grown sample exhibits the intended uniaxial magnetocrystalline anisotropy and macrospin behavior, in-plane magnetic hysteresis loops have been measured by means of a vibrating sample magnetometer (VSM) system. This VSM tool allows the sample to be rotated, with the rotation axis being the surface normal, so that the field is always in the surface plane, and correspondingly, the magnetization vector is always within the surface plane. The specific orientations of the EA and the magnetization with respect to the applied field direction are defined by angles $\varphi_0$ and $\varphi_m$ in this case, as indicated by the macrospin model representation in Fig. 2(b). Experimentally, we have measured complete VSM hysteresis loops for different $\varphi_0$ values, such as the ones represented in Fig. 2(c) and compiled the corresponding data. The results shown in Fig. 2(c) exhibit hereby the nearly perfect textbook behavior for a uniaxial magnetic material showing a squarelike hysteresis loop along the EA ($\varphi_0 = 0°$) and a hysteresis-free gradual reversal along the magnetic hard axis (HA; $\varphi_0 = 90°$). For an unambiguous visualization and demonstration of the macrospin behavior of our sample, we have performed a full 360° scan of $\varphi_0$ values by measuring the type of hysteresis loop shown in Fig. 2(c) for each $\varphi_0$ value. Figure 2(d) shows as a color-coded map the results of these measurements by displaying the normalized in-plane magnetization $M/M_s$ along the field direction that was measured from saturation to remanence as a function of the applied magnetic field strength $H$ and angle $\varphi_0$. For high fields, the magnetization is saturated for all angles, and $M/M_s = 1$. For low fields, $M/M_s$ approaches zero

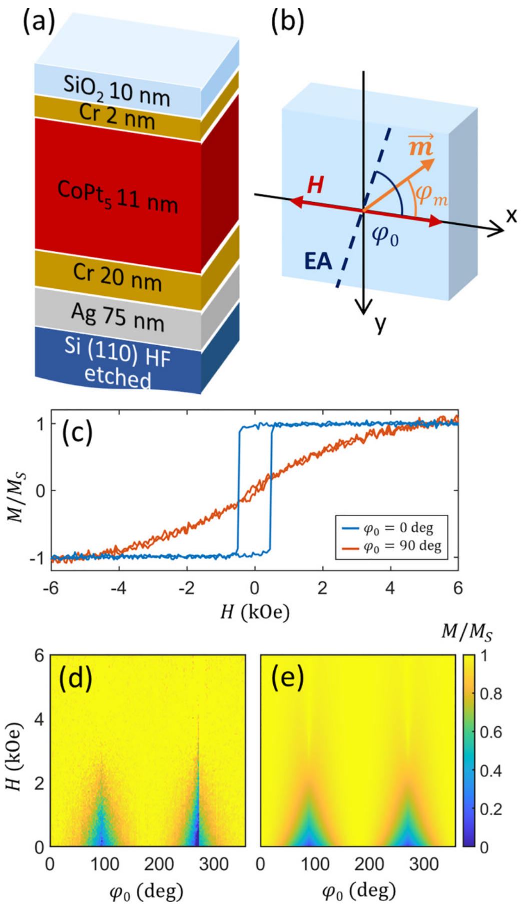


FIG. 2. (a) Schematic of the fabricated sample, indicating the thickness of the layers (not to scale), consisting of the epitaxial film sequence Ag(110)/Cr(211)/$CoPt_{0.05}(10\bar{1}0)$/Cr(211), grown onto a Si(110) substrate, whose oxide has been removed by hydrofloric acid etching. The sample is covered by a 10-nm-thick $SiO_2$ layer to avoid oxidation. (b) Representation of the geometry of the macrospin model for thin films including the definition of $\varphi_0$ being the angle between the external magnetic field axis and the uniaxial easy axis (EA) orientation of the sample and $\varphi_m$ being the in-plane angle that the magnetization vector $\vec{m}$ forms with the magnetic field axis. (c) $M/M_S$ vs $H$ hysteresis loops for two $\varphi_0$ values, namely, $\varphi_0 = 0^\circ$ and $90^\circ$, showing the EA and hard axis (HA) behavior of our sample. (d) Color-coded map of the normalized magnetization $M/M_S$ along the applied field direction, measured by means of vibrating sample magnetometer (VSM), as a function of $\varphi_0$ and the field strength $H$, for the sample displayed in (a). (e) Corresponding least-squares fit of the data based upon the minimization of the total energy according to Eq. (6). The color-code legend at the right side of (e) applies to both (d) and (e).

if $\varphi_0 = 90^\circ$ or $270^\circ$ but remains equal to $\sim 1$ for $\varphi_0 = 0^\circ$ or $180^\circ$. Moreover, for $0^\circ$ and $180^\circ$, the $M/M_s$ variation with $H$ is negligible, given that $M$ is saturated along those directions even at remanence. The $180^\circ$ periodicity of the data pattern confirms that the sample shows marked uniaxial magnetic anisotropy, which we wanted to verify. Also, centered around $\varphi_0 = 90^\circ$ and $270^\circ$, one can observe a cone-shaped structure of reduced magnetization. This cone structure is defined by an angular-dependent saturation field for any orientation that is not the EA. Specifically, along $\varphi_0 = 90^\circ$ and $270^\circ$, larger fields are required to induce a magnetization rotation toward the field direction, which is the behavior expected along the HA orientation of the magnetic field. Therefore, with the designed sample, the magnetization will rotate from being parallel to the external field at high field values to an EA orientation when no external field is applied.

Least-squares fits of the $M/M_s(H, \varphi_0)$ data to a macrospin model have been done to establish that a single macrospin describes the complete field dependence of the sample magnetization for any in-plane magnetic field orientation. The corresponding free energy expression of in-plane uniaxial magnetic films has been used [49,50]:

$$E = -\mu_0 M_s H \cos(\varphi_m) + k_1 \sin^2(\varphi_0 - \varphi_m) + k_2 \sin^4(\varphi_0 - \varphi_m), \quad (6)$$

in which the first- and second-order magnetocrystalline anisotropy constants are given by $k_1$ and $k_2$, respectively. These two constants $k_1$ and $k_2$ and the saturation magnetization $M_s$ are the only fit parameters used for the map, and the values obtained for our sample are $k_1 = 0.913 \times 10^6$ erg/cm$^3$, $k_2 = 0.632 \times 10^6$ erg/cm$^3$, and $M_s = 901$ emu/cm$^3$, which are in line with other Co-alloy films that we have fabricated using the same type of deposition process and underlayer structure [45]. The second-order anisotropy constant has been included here since it is well known that its value is sufficiently large in Co-alloy material systems [50]. Figure 2(e) shows the fit result of our $M/M_s(H, \varphi_0)$ data to Eq. (6), which exhibits excellent agreement with the corresponding experimental data in Fig. 2(d). Thus, it confirms the uniaxial and macrospin behavior of our epitaxial film sample, demonstrating that, in our sample, a wide range of magnetization orientation states is easily accessible, all exhibiting a magnetization vector of constant length.

### B. GME

The method that we have used to experimentally obtain the full reflection matrix **R** is GME, whose details are discussed in Refs. [16,29,51] and whose main advantage it is that one can obtain all reflection matrix elements in a single measurement sequence. Another strength of this methodology is that all MOKE components can be separated from each other in a very robust manner [52]. The experimental setup used in this paper is schematically represented in Fig. 3. In Fig. 3(a), from left to right, the components of our GME setup are a laser source, a first linear polarizer $P_1$, the sample to be measured between the coils of an electromagnet, a second linear polarizer $P_2$, and a photodetector. As a laser source, we use a linearly polarized and intensity stabilized low-noise solid-state laser that emits light at a wavelength of 635 nm. The first linear polarizer, located in the incident beam path, defines the linear polarization axis of the incident light by means of angle $\theta_1$, in reference to the *s*-polarization direction, which is perpendicular to the plane of incidence. The linearly polarized light is reflected by the sample, and after reflection, the light passes through the second linear polarizer $P_2$, whose linear polarization axis is defined by angle $\theta_2$, also in reference to the *s*-polarization direction. Finally, the transmitted light intensity $I$, after passing through $P_2$, is measured with a Si-photodiode detector. Positive values of the linear polarizer angles $\theta_1$ and

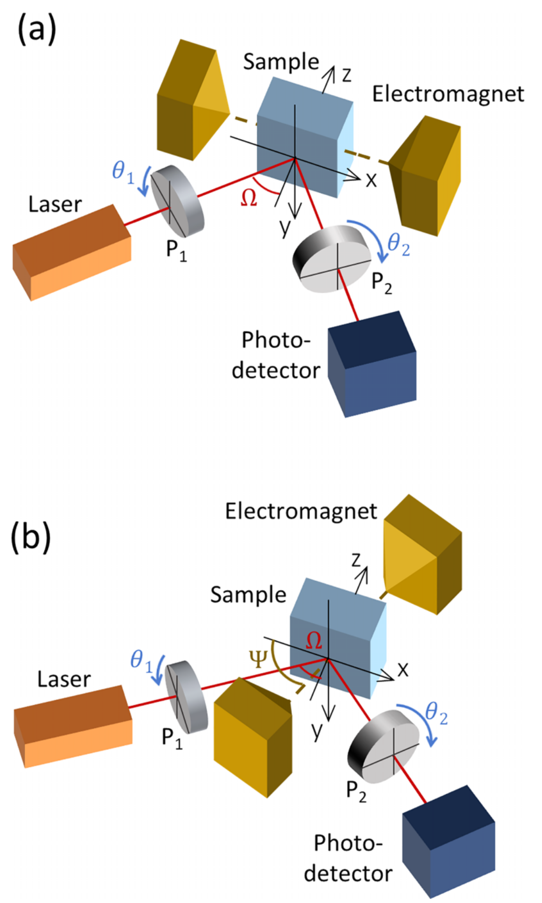


FIG. 3. Schematic of the generalized magneto-optical ellipsometry (GME) experimental setup in the (a) in-plane and (b) out-of-plane geometries, consisting of a laser light source, a first polarizer $P_1$, a second polarizer $P_2$, and a photodetector. The polarization angles $\theta_1$ for $P_1$ and $\theta_2$ for $P_2$ are given as the angular distance between the axis of each optical element and the *s*-polarization direction, utilizing the displayed sign convention (blue arrows) indicating the positive rotation sense. The sample under investigation is located inside the gap of an electromagnet that produces a magnetic field contained in the optical plane of incidence, which is also aligned with the sample plane in (a), while it has an angle of $\Psi = 87^\circ$ with the sample plane in (b). The path of the light beam is represented by the red line, having an angle of incidence of $\Omega = 26^\circ$ for the in-plane geometry and $\Omega = 70^\circ$ for the out-of-plane geometry with respect to the surface normal.

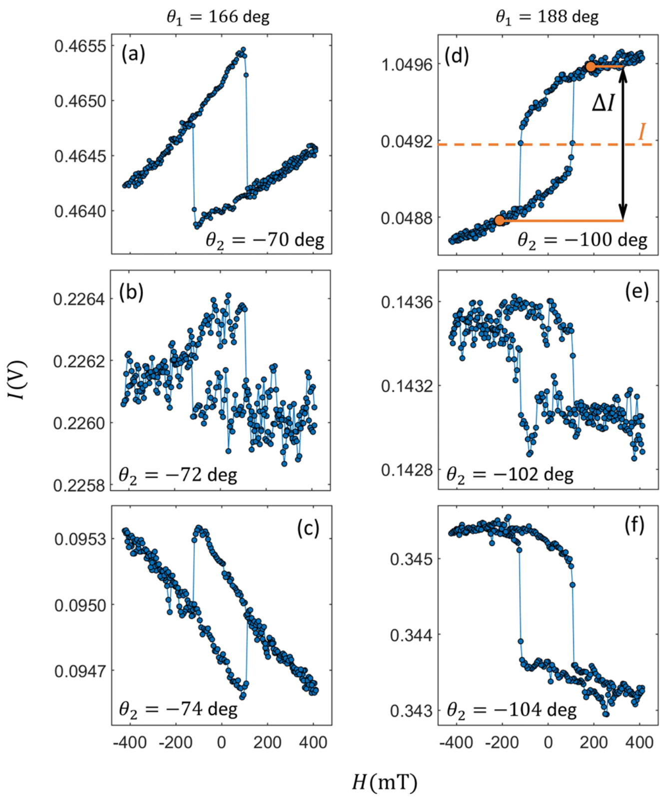


FIG. 4. Exemplary generalized magneto-optical ellipsometry (GME)-type light intensity $I$ vs $H$ hysteresis loops for different ($\theta_1$, $\theta_2$) settings. (a)–(c) correspond to the same $\theta_1$ value of 166°, while $\theta_2$ is −70°, −72°, and −74°, respectively, in each subfigure. Equally, (d)–(f) correspond to the same $\theta_1$ value of 188°, while $\theta_2$ is −100°, −102°, and −104° in the respective subfigure. The intensity difference $\Delta I$ corresponding to a fixed $H$ and $-H$ value pair and the mean intensity for those two points $I$ are illustrated in (d).

$\theta_2$ are associated with the counterclockwise rotation sense along the propagation direction of the light, as indicated in Fig. 3(a) by the blue arrows. The two linear polarizers are set onto motorized rotation stages, which allows one to set the orientations of the polarizers reproducibly with high angular precision.

In the in-plane magnetization case, the electromagnet produces an external magnetic field along the longitudinal orientation, as represented in Fig. 3(a). The laser is positioned in our setup so that the angle of incidence is $\Omega = 26^\circ$, which represents a compromise between obtaining good sensitivity and the ability to achieve a reasonably high magnetic field in the longitudinal direction. The setup geometry that enables us to access a predominant out-of-plane orientation of the external magnetic field direction is represented in Fig. 3(b). The experimental setup contains the same elements, and the already defined light path and angle definitions are also identical. The main difference is the electromagnet orientation, as it has been rotated to obtain a very large out-of-plane magnetic field component, for the purpose of facilitating substantial levels of out-of-plane magnetization values in combination with simultaneously varying in-plane components. Specifically, the angle of rotation of the electromagnet with respect to the sample surface is $\Psi = 87^\circ$, and the angle of incidence of the laser light with respect to the surface normal is $\Omega = 70^\circ$ in this case. These angles were chosen as the most convenient for obtaining the best sensitivity while also giving us the ability to achieve a magnetic field contained in the optical plane-of-incidence but with a high out-of-plane component.

In the GME methodology, the transmitted light intensity is measured at the photodetector as a function of the applied magnetic field $H$ for a defined ($\theta_1$, $\theta_2$) pair setting, upon which the measurement is then repeated multiple times for a series of different ($\theta_1$, $\theta_2$) pairs. Figure 4 shows several selected examples of such measurements for different ($\theta_1$, $\theta_2$) pair settings, measured on our Co-Pt alloy sample in the experimental configuration of Fig. 3(a) using $\varphi_0 = 78.75^\circ$. All six curves in Fig. 4 display a MOKE measurement of the hysteresis loop of

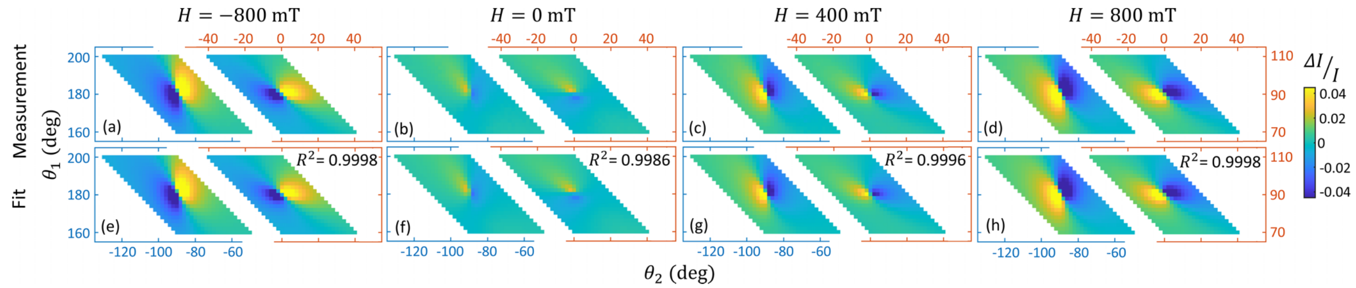


FIG. 5. (a)–(d) Sequence of experimentally measured $\Delta I/I(\theta_1,\ \theta_2)$ color-coded maps obtained for four different fields, namely, $H = -800$, 0, 400, and 800 mT, and (e)–(h) the corresponding fits to Eq. (8), with the $R^2$ value displayed in the right top corner of every subfigure. The data correspond to measurements on the sample represented in Fig. 2(a) with the generalized magneto-optical ellipsometry (GME) setup shown in Fig. 3(b). The two color-coded maps contained in each subfigure show data around the $s-p$ (left map, blue axis) and $p-s$ (right map, orange axis) crossing-point configurations of the polarizers. The color-scale on the right side of the figure applies to all subfigures.

our sample, but the appearance of the actual signal trajectory is quite different for different $(\theta_1,\ \theta_2)$ pairs. While the magnetization switching at the coercive field always occurs at the same field value since the sample itself undergoes the same magnetization reversal process in each case, independent from the specific $(\theta_1, \theta_2)$ pair setting, the hysteresis loop shapes and amplitudes vary greatly. Also, the sign of the MOKE-induced light intensity change reverses as the polarizer settings are modified, which is very visible if one compares Fig. 4(a) with 4(c) or Fig. 4(d) with 4(f), respectively. Also, the total detected light intensity $I$ varies very significantly as the $(\theta_1,\ \theta_2)$ pair settings are modified. These differences are associated with the different ellipsometric detection conditions in each case, which is exactly the strategy with which GME enables the complete determination of the full reflection matrix **R**.

From each full hysteresis loop dataset, the normalized intensity changes between the applied fields $H$ for the decreasing field branch and $-H$ for the increasing field branch are determined, given that these measurement points represent inverted magnetic states. The intensity change $\Delta I$ as well as the mean intensity $I$, for a specific $H$ value, is indicated in Fig. 4(d). Formally, one can express this quantity as

$$\frac{\Delta I}{I}(H) = 2\frac{I(H) - I(-H)}{I(H) + I(-H)}. \tag{7}$$

This data extraction is then repeated for a grid of orientations of the polarizer settings $(\theta_1,\ \theta_2)$. The $(\theta_1,\ \theta_2)$ grids are specifically chosen to obtain the best sensitivity for the small MO effects, creating a diagonally shaped $\Delta I/I$ map for every magnetic field value [52]. Furthermore, to achieve an unambiguous separation of L- and P-MOKE signals, two grid segments are needed, which are ideally placed in the vicinity of the extinction points defined by the $s-p$ and $p-s$ configurations of the two polarizers.

With the help of $\Delta I/I$ datasets, it is now possible to determine the entire reflection matrix, given that an equation for the normalized intensity changes due to magnetization inversion has been derived previously [29,51]:

$$\frac{\Delta I}{I}(H,\theta_1,\theta_2) = 4\frac{B_1 f_1 + B_2 f_2 + B_3 f_3 + B_4 f_4 + B_5 f_5 + B_6 f_6}{f_3 + B_7 f_7 + 2B_8 f_4 + I_0}, \tag{8}$$

in which $f_i(\theta_1, \theta_2)$ are known trigonometric functions [51] and $B_i(H)$ are parameters related to the components of the reflection matrix, specifically $B_1 = \mathrm{Re}(\tilde{\alpha})$, $B_2 = \mathrm{Re}(\widetilde{r_s}\,\tilde{\alpha}^*)$, $B_3 = \mathrm{Re}(\tilde{\beta})$, $B_4 = \mathrm{Re}(\widetilde{r_s}\,\tilde{\beta}^*)$, $B_5 = \mathrm{Re}(\tilde{\gamma})$, $B_6 = \mathrm{Re}(\widetilde{r_s}\,\tilde{\gamma}^*)$, $B_7 = |\widetilde{r_s}|^2$, and $B_8 = \mathrm{Re}(\widetilde{r_s})$. The additional term $I_0$ in Eq. (8) is a small experimental correction term that accounts for a background intensity due to very small imperfections of the optical elements. Using this expression as a function of the two linear polarizer angles, $B_i$ and $I_0$ are obtained as fitting parameters for all $\Delta I/I(H)$ measured maps. The full derivation and explicit functional forms of Eq. (8) can be found in Refs. [29,51].

The color-coded maps in Figs. 5(a)–5(d) represent experimentally measured $\Delta I/I$ data, with the horizontal axis given by $\theta_2$ values and the vertical axis accordingly defined by $\theta_1$. These exemplary maps correspond to measurements on our Co-Pt alloy film sample with the GME setup displayed in the out-of-plane configuration, shown in Fig. 3(b). The sample is oriented with $\Psi = 87^\circ$ and $\varphi_0 = 45^\circ$ so that all magnetization components are present. Figures 5(a)–5(d) correspond to different magnetic field strength values $H$ as indicated at the top of each column. Moreover, each subfigure contains two color-coded maps for the two measurement grids around the $s-p$ and $p-s$ crossing points of the polarizers. One can observe that the pattern changes as the magnetic field strength increases, and the magnetization vector rotates accordingly. This change is not only caused by a difference in the signal intensity but also by a change of the shape of our signal pattern. For $H = -800$ mT in Fig. 5(a), one can see two well-defined peaks of opposite sign, symmetrically placed around the diagonal of the grid and with the positive peak having slightly bigger absolute values. For $H = 0$ mT in Fig. 5(b), the intensity of the $\Delta I/I$ signal of the peaks is reduced, and the symmetry of the peaks has changed from a dominant diagonal symmetry axis to a signal pattern that is more aligned with the vertical and horizontal axes for the $s-p$ and $p-s$ maps, respectively. For $H = 400$ mT in Fig. 5(c), the peak intensities increase again and continue increasing for $H = 800$ mT in Fig. 5(d), hereby exhibiting very similar intensities as for the $H = -800$ mT case but with inverted peaks as the magnetization itself is inverted. The least-squares fit results to Eq. (8) are represented in the second row of Fig. 5, each subfigure being the corresponding simultaneous fit result of the above measured color-coded maps. The $R^2$

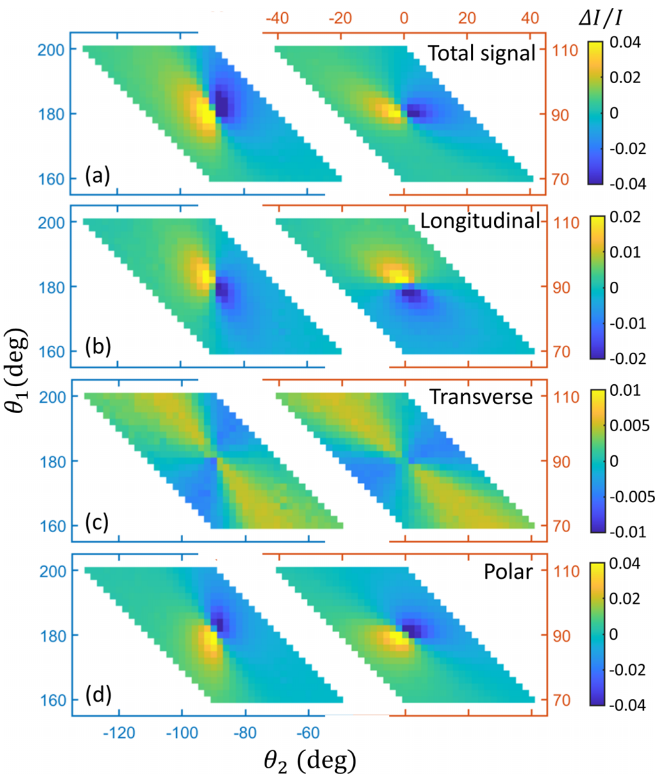


FIG. 6. Experimental $\Delta I/I$ color-coded maps obtained for $H = 400$ mT, displaying the (a) total signal as well as the correspondingly extracted (b) longitudinal, (c) transverse, and (d) polar signals, as indicated in the top right corner of each subfigure. The color code for each subfigure is shown on its right-hand side and is adapted to the size of each signal component.

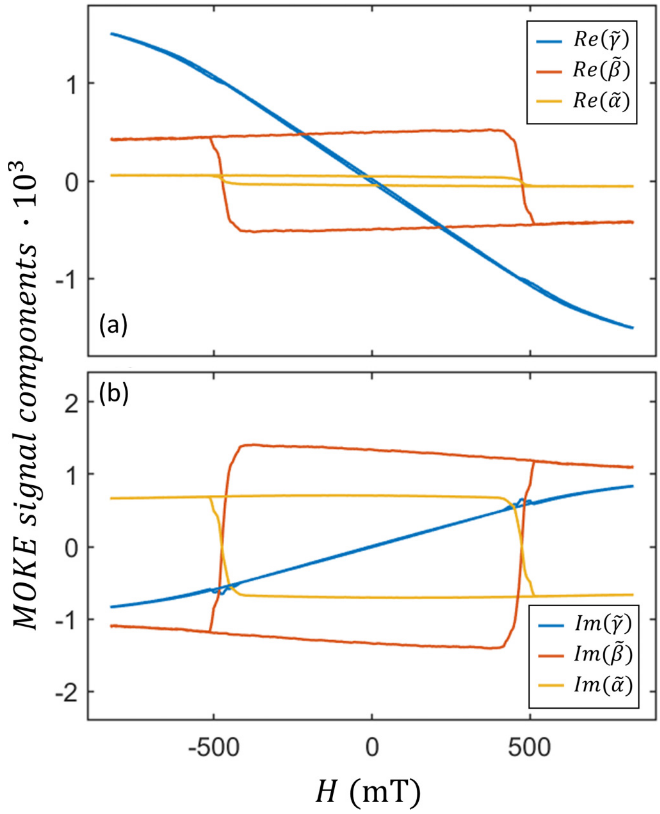


FIG. 7. Applied field $H$ evolution of (a) the real part and (b) the imaginary part of the magneto-optical Kerr effect (MOKE) parameters $\tilde{\alpha}$, $\tilde{\beta}$, and $\tilde{\gamma}$. Data were measured on the sample displayed in Fig. 2(a) for an out-of-plane configuration of the generalized magneto-optical ellipsometry (GME), as shown in Fig. 3(b) with an in-plane orientation of the sample of $\varphi_0 = 45^\circ$.

values of the corresponding fits are shown in the top-right corner of the individual subfigures, and in all cases, their values are $> 0.998$, which confirms the visual impression of the fit results replicating the experimental data extremely well, which in turn ensures that the obtained fit parameters are very reliably determined.

The specific reason why all three MOKE components can be separated from each other in a very robust manner is the fact that L-, T-, and P-MOKE exhibit different symmetries in the signal pattern with respect to $\theta_1$ and $\theta_2$ [51]. We can see the different symmetries in Fig. 6, where Fig. 6(a) shows the total measured signal as already represented in Fig. 5(c), and Figs. 6(b)–6(d) the associated extracted longitudinal, transverse, and polar signals, respectively, as indicated in the top-right corner of each subfigure. The transverse signal shows symmetric behavior with respect to the extinction points, while longitudinal and polar signals are antisymmetric at those points. To distinguish polar and longitudinal effects accurately, it is necessary to have the two maps representing the vicinity of both the $s-p$ and $p-s$ crossing points as the differences between those segments are distinct: in Fig. 6(b), the longitudinal signal has the positive peak on the upper area of the $(\theta_1, \theta_2)$ grid and the negative peak on the lower area, while in Fig. 6(d), for the polar, the positive and negative peaks are distributed in a left-right manner [51,53].

The data acquisition method and the data analysis that we show in an exemplary fashion in Figs. 5 and 6 are repeated for every applied field value of a hysteresis cycle, and thus, we can extract the full reflection matrix according to Eq. (1) for every field value. In this way, the field evolution of the MO parameters can be followed as represented in Fig. 7. Specifically, in Fig. 7(a), one can see the behavior of the real part of $\tilde{\alpha}$, $\tilde{\beta}$, and $\tilde{\gamma}$ vs the applied magnetic field for the same sample and conditions as in Figs. 5 and 6, and in Fig. 7(b), the corresponding behavior of the imaginary parts of $\tilde{\alpha}$, $\tilde{\beta}$, and $\tilde{\gamma}$ is shown. The polar component changes linearly with the field strength for sufficiently low field values while beginning to show a transition into sublinear behavior for higher field values. On the other hand, the in-plane magnetization components change only slightly except for the magnetization inversion at the coercive field, for which we observe the abrupt change characteristic of a sharp hysteresis loop. The small variation of the in-plane magnetization-related components $\tilde{\alpha}$ and $\tilde{\beta}$ with field, best observed in Fig. 7(b) for the imaginary part of $\tilde{\beta}$ but present in the real and imaginary parts of both in-plane components, is associated with a decrease of the in-plane projection of the magnetization vector as the out-of-plane component increases. Moreover, there is a small rotation of the in-plane magnetization projection, which we wanted to generate as well. In the case of the MOKE-parameter field evolution for the in-plane magnetization setup geometry, shown in Fig. 3(a), all the magnetization rotation happens within the film plane, as no polar effect is present. The in-plane field component is much larger in this case, and thus, there are far larger in-plane magnetization rotations against the in-plane anisotropy, covering a broader angular range of $\varphi_m$, which means that both the real and imaginary parts of $\tilde{\alpha}$ and $\tilde{\beta}$ exhibit bigger variations in addition to magnetization inversion effects.

## III. EXPERIMENTAL RESULTS

### A. Experimental verification for in-plane magnetization cases

We have first determined the reflection matrices for cases of in-plane magnetization states, including L- and T-MOKE signal components but no polar effect, as a function of $H$. For the in-plane magnetization case, the setup utilized is the one described in Fig. 3(a). Here, we want to obtain a wide angular range of magnetization vector orientations to obtain a truly rigorous test for the correlation between the two in-plane MO components as defined by Eqs. (2) and (3). Therefore, we perform measurements near the HA orientation of our sample, and in addition, we use a certain number of slightly different orientations to acquire multiple separate and independent datasets. In these measurements, the magnetization vector aligns with the EA when no field is applied, and as the field strength increases, the magnetization rotates to align with the field orientation, applied along the longitudinal direction, overall covering a rotation of the magnetization from an almost purely transverse signal to a predominantly longitudinal case.

For four different $\varphi_0$ angles, namely, $\varphi_0 = 96.25^\circ$, $91.25^\circ$, $88.75^\circ$, and $86.25^\circ$, GME measurements have been performed and analyzed for many field values. For the following quantitative discussion of our measured data, we will utilize only the experimental results, for which stable macrospin-type magnetization states are realized, even if GME measurements were made and analyzed for all field values and cover the entirety of hysteresis loops. By doing so, we are assured that the magnetic sample state is laterally uniform, does not exhibit domains, and is characterized by only one uniform magnetization vector and therefore makes a quantitative data interpretation in terms of Eq. (1) meaningful. To ensure that these macrospin conditions are fulfilled, only measurements are analyzed from the maximum applied magnetic field strength down to remanence. Figure 8(a) displays the resulting MO data, particularly the relation between the absolute values of $\tilde{\alpha}$ and $\tilde{\beta}$. If Eq. (2) is correct, which is a necessary condition for Eq. (1) to be correct, these data should fall onto an ellipse, and indeed, we see that they do. The data furthermore demonstrate that all four measurement sets for different sample orientations $\varphi_0$ follow the same ellipse relation, which is exactly the expected result according to Eqs. (1) and (2), given that the MO reflection matrix elements should not explicitly depend on the EA orientation $\varphi_0$. Error bars are not shown in Fig. 8(a), given that all error values are smaller than the individual dot sizes, illustrating that Eq. (8) describes experimental $\Delta I/I$ GME data with great accuracy. Figure 8(b) represents the phases of $\tilde{\alpha}$ and $\tilde{\beta}$, which within the error bars, all collapse onto one point, as predicted by Eq. (3), which is further confirmation of the accuracy of Eq. (1). Finally, the analyzed data for the purely optical parameter $\tilde{r}_s$ are displayed in Fig. 8(c), with the vertical axis being the imaginary component and the horizontal axis its real component. Also in this plot, the resulting data points fall on top of each other, confirming that the pure optical parameter $\tilde{r}_s$ is independent from the magnetization orientation, thus reaffirming the structure of **R** according to Eq. (1), which has clearly separated MO and purely optical elements. Thus, our entire set of in-plane magnetization data is not only fully consistent with Eq. (1) but confirms the derived relations for the in-plane MOKE effect to a very high degree of precision, with average deviations being $<0.7\%$ of the respective full transverse or longitudinal effects.

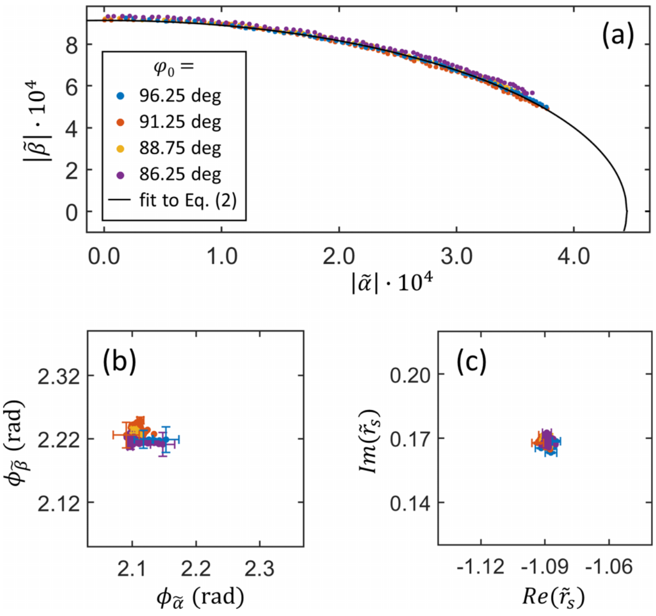


FIG. 8. (a) Experimental data for $|\tilde{\beta}|$ vs $|\tilde{\alpha}|$ measured by using the in-plane generalized magneto-optical ellipsometry (GME) geometry according to Fig. 3(a) for four different sample orientations $\varphi_0$, in comparison with the expected functional behavior, Eq. (2); (b) $\phi_{\tilde{\beta}}$ vs $\phi_{\tilde{\alpha}}$ and (c) Re($\tilde{r}_s$) vs Im($\tilde{r}_s$) for the same datasets shown in (a). In subfigures (b) and (c), not all error bars are displayed for the purpose of clarity.

### B. Experimental verification for arbitrary magnetization orientations

For the most general magnetization orientation cases, an additional out-of-plane magnetization component and associated P-MOKE exists, as described by means of Eqs. (4) and (5), which were also derived from Eq. (1). Thus, like the in-plane magnetization case, we have utilized the GME methodology to generate several datasets, such as the one shown in Fig. 5, and determined the reflection matrix parameters for each applied magnetic field value. For this, we utilized the GME setup represented in Fig. 3(b) to obtain relevant levels of out-of-plane magnetization. In all our measurements, $\Psi$ and $\Omega$ were kept fixed at the values described above, and several datasets were taken for different in-plane orientations $\varphi_0$ to enable a relevant variation of the magnetization vector

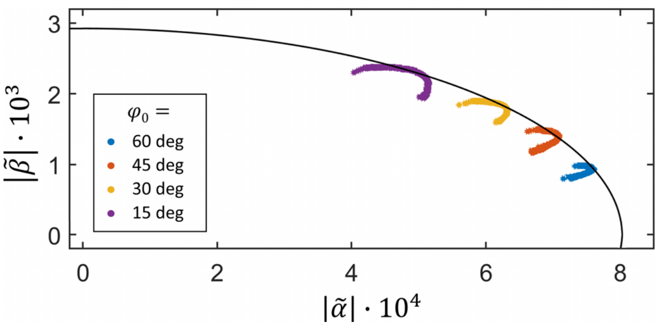


FIG. 9. (a) Experimental data for $|\tilde{\beta}|$ vs $|\tilde{\alpha}|$ measured by using the out-of-plane generalized magneto-optical ellipsometry (GME) geometry according to Fig. 3(b) for four different sample orientations $\varphi_0$, in comparison with the expected in-plane functional behavior, Eq. (2); the line represents the ellipse equation boundary, which is tangential to the data.

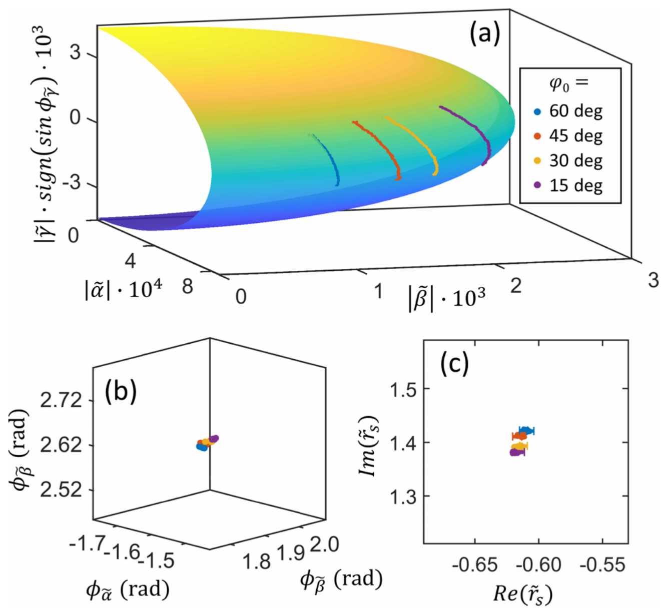


FIG. 10. (a) Projection of the three-dimensional (3D) behavior of the relation between $|\tilde{\alpha}|$, $|\tilde{\beta}|$, and $|\tilde{\gamma}|$ for out-of-plane generalized magneto-optical ellipsometry (GME) measurements made for four different $\varphi_0$ angles; the ellipsoid surface is obtained from a least-squares fit of the experimental data to Eq. (4); (b) quasi-3D plot of $\phi_{\tilde{\alpha}}$, $\phi_{\tilde{\beta}}$, and $\phi_{\tilde{\gamma}}$ for all measured data points; (c) $\mathrm{Re}(\tilde{r}_s)$ vs $\mathrm{Im}(\tilde{r}_s)$ data obtained for the entire measurement set.

orientation and thus rigorous testing of Eq. (1). Specifically, four different in-plane sample orientations were measured, namely, $\varphi_0 = 60^\circ$, $45^\circ$, $30^\circ$, and $15^\circ$. The relation between the measured absolute values of $\tilde{\alpha}$ and $\tilde{\beta}$ for these four sample orientations is displayed in Fig. 9, and as we can see in this three-dimensional (3D) magnetization case, $|\tilde{\alpha}|$ and $|\tilde{\beta}|$ are no longer correlated by means of the ellipse equation, Eq. (2). However, the four datasets exhibit a tangential relationship to the ellipse equation, as shown comparatively in Fig. 9. This is due to the reduction of the in-plane projection of the magnetization as it rotates out of plane. Instead, $|\tilde{\alpha}|$, $|\tilde{\beta}|$, and $|\tilde{\gamma}|$ must be related by the ellipsoid equation, Eq. (4), to be consistent with the form of **R** in Eq. (1) for the most general magnetization orientation scenario, and indeed, our experimental data follow Eq. (4) very precisely, as one can see in the 3D projection plot in Fig. 10(a), where the four lines represent the measured data for the four different in-plane orientations $\varphi_0$, and the surface represents the ellipsoid fit result. The mean relative error between the data and the ellipsoid fit result is <2.5% for all four datasets. The ellipse equation that encircles the data in Fig. 9 corresponds hereby to the equatorial ellipse of the ellipsoid. The relations between the phases $\phi_{\tilde{\alpha}}$, $\phi_{\tilde{\beta}}$, and $\phi_{\tilde{\gamma}}$ are represented in Fig. 10(b). As one can see, all the data points collapse onto one point, in agreement with the derived condition, Eq. (5). Finally, the resulting purely optical parameters are analyzed and displayed in Fig. 10(c), which leads us to the same conclusion that we obtained in conjunction with Fig. 8(c), namely, the optical parameter $\tilde{r}_s$ remains independent from the applied magnetic field and sample magnetization state. However, the collapse is not quite as good as in the case of the pure in-plane magnetization data in Fig. 8(c), which is related to the much larger range of in-plane orientation angles $\varphi_0$ here in conjunction with optical anisotropy that can occur in oxide overcoats on top of epitaxial metal films [54]. This explanation is also consistent with the fact that the variation within each set of data for fixed $\varphi_0$ is far smaller than between the datasets. All our findings here are fully consistent in a quantitatively precise manner with Eqs. (4) and (5) and thus Eq. (1).

One may notice the very different numerical values in Figs. 9 and 10 if compared with Fig. 8. For example, the maximum value of $\tilde{\beta}$ is $\sim 3 \times 10^{-3}$ in Figs. 9 and 10(a), while it is only $\sim 9 \times 10^{-4}$ for the in-plane case in Fig. 8(a). There are also numerical differences if one compares the phase values and the pure optical parameter $\tilde{r}_s$ between Figs. 8 and 10. These differences are due to the two very different angles of incidence that were used for the corresponding measurements, being $\Omega = 70^\circ$ for the general magnetization case (Figs. 9 and 10) and $\Omega = 26^\circ$ for the in-plane magnetization case (Fig. 8).

### C. Deviations due to MO anisotropy

Previously reported deviations from Eq. (1) [39–41,55] were associated with a lack of isotropy in the MO coupling constant in anisotropic single-crystal samples. Thus, they might exist in our uniaxial sample as well and could lead to deviations under certain conditions. In this subsection, we explore and verify that we can detect those deviations, which also confirms the precision and general viability of our experimental approach. For these experiments, we utilized the same sample but selected measurement conditions that are expected to produce relevant levels of MO anisotropy effects. Specifically, we utilize the in-plane magnetization configuration but rotate the sample farther away from the HA configuration, i.e., we use relevantly smaller $\varphi_0$ values. In this case, the MOKE elements of **R** can exhibit an anomalous magnetization dependence [55], such as, for instance, having the longitudinal term $\tilde{\alpha}$ of Eq. (1) as a linear combination of $m_x$ and $m_y$, namely,

$$\tilde{\alpha} = \tilde{\alpha}_L \cdot m_x + \tilde{\alpha}_T \cdot m_y, \tag{9}$$

with $\tilde{\alpha}_L$ and $\tilde{\alpha}_T$ being the linear coefficients for the conventional longitudinal and the anomalous transverse

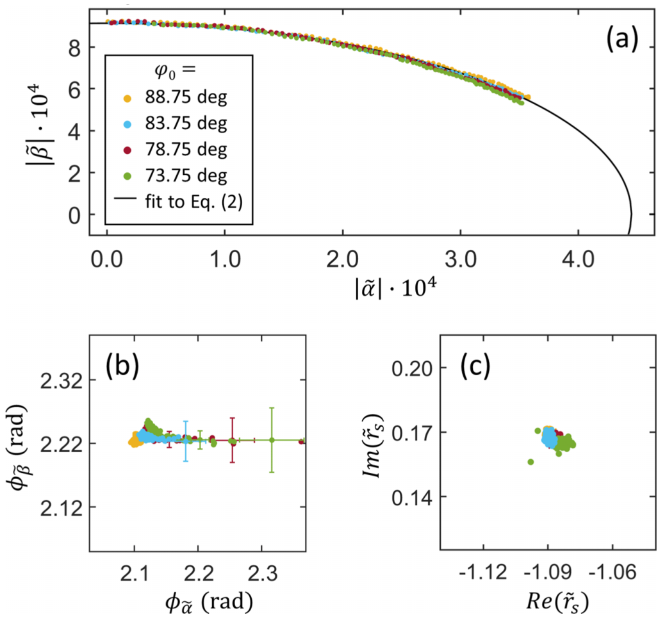


FIG. 11. (a) Representation of the relation between $|\tilde{\beta}|$ and $|\tilde{\alpha}|$, for the in-plane generalized magneto-optical ellipsometry (GME) geometry for a different set of $\varphi_0$ angles, plus the fit function of the data to Eq. (2); (b) $\phi_{\tilde{\beta}}$ vs $\phi_{\tilde{\alpha}}$ and (c) Re($\tilde{r}_s$) vs Im($\tilde{r}_s$) for the same datasets shown in (a). In subfigures (b) and (c), not all the error bars are displayed for the purpose of clarity.

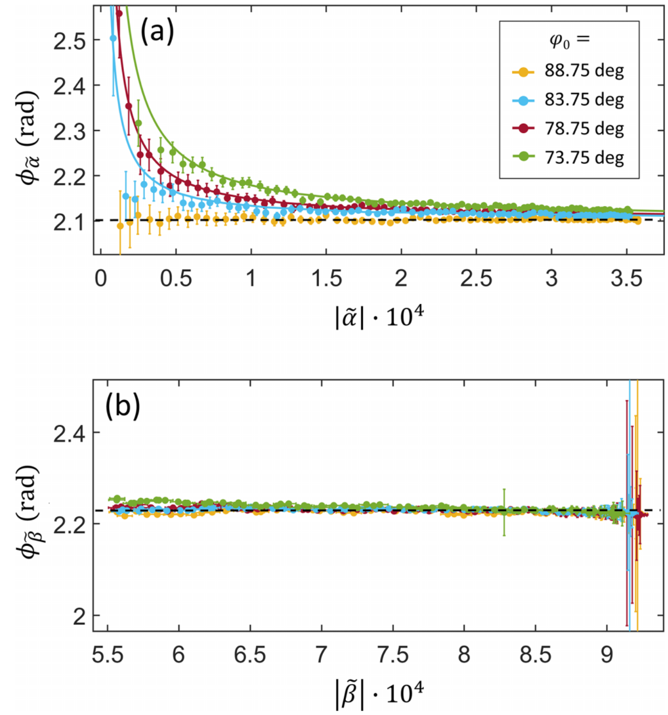


FIG. 12. Experimental data, measured for the in-plane generalized magneto-optical ellipsometry (GME) geometry, representing (a) $\phi_{\tilde{\alpha}}$ vs $|\tilde{\alpha}|$, with the lines corresponding to fitting the data to Eq. (9) and (b) $\phi_{\tilde{\beta}}$ vs $|\tilde{\beta}|$, for a set of sample orientations $\varphi_0$. The dashed lines in (a) and (b) represent constant values of $\phi_{\tilde{\alpha}}$ and $\phi_{\tilde{\beta}}$, respectively, and act as guides to the eye.

magnetization signals. For our experiments, we used the same procedure that was described in Sec. III A but utilize $\varphi_0$ angles much farther away from the HA configuration, specifically $\varphi_0 = 88.75^\circ$, $83.75^\circ$, $78.75^\circ$, and $73.75^\circ$. After the proper analysis of our GME measurements using Eqs. (7) and (8), the reflection matrix parameters are extracted. The corresponding correlation relation between $|\tilde{\alpha}|$ and $|\tilde{\beta}|$ is represented in Fig. 11(a), where the ellipse equation fits the data as predicted by Eq. (2). However, we see in Fig. 11(b) that the phase of $\tilde{\alpha}$ does not remain constant, thus not fulfilling the second test condition given by Eq. (3). On the other hand, the optical parameters remain constant, as shown in Fig. 11(c). The anomalous magnetization state dependence of $\phi_{\tilde{\alpha}}$ would impact the accuracy of MOKE measurements, if data were not properly interpreted, given that it is associated with a deviation from Eq. (1).

We represent in Fig. 12(a) the phase of $\tilde{\alpha}$ as a function of its absolute value, which allows us to visualize the existing deviations in a systematic fashion. The lines are the resulting fits to Eq. (9), which follow the experimentally determined values very well. As we can see, the deviation from a constant $\phi_{\tilde{\alpha}}$ value gets larger for smaller $|\tilde{\alpha}|$ values, as they correspond to magnetization states which have a small $m_x$ component and correspondingly a very large and dominating $m_y$ component. The anomalous prefactor of the transverse magnetization component $\tilde{\alpha}_T$ is rather small, but once $m_x$ gets very small in comparison with $m_y$, the second term in Eq. (9) can contribute relevantly. Given that both $\tilde{\alpha}_T$ and $\tilde{\alpha}_L$ prefactors can have different phases, the overall $\phi_{\tilde{\alpha}}$ changes with the magnetization state, which is exactly what the data show, if one is sufficiently far away from the HA field orientation. Moreover, this $\phi_{\tilde{\alpha}}$ dependency from the magnetic state decreases as $\varphi_0$ aproaches $90^\circ$, which leads to a full restoration of the exactness of Eq. (1) for $\varphi_0 = 0^\circ$, $\pm 90^\circ$, and $180^\circ$ because, in this case, the independent and crystallographically defined MO constants apply exclusively to the L- and T-MOKE, respectively, without intermixing [55]. This also explains why the deviation was not observed in Fig. 8, given that all the selected sample orientations were close to $\varphi_0 = 90^\circ$. Measurements for even smaller $\varphi_0$ angles are not shown in Fig. 12 because the rotation range of the magnetization vector is quite small in this case and furthermore does not allow for the generation of small $\tilde{\alpha}$ values due to hysteretic switching. This is presumably also the reason why we do not observe a similar effect for $\tilde{\beta}$ in Fig. 12(b). Fundamentally, the transverse component $\tilde{\beta}$ is expected to follow the relation:

$$\tilde{\beta} = \tilde{\beta}_L \cdot m_x + \tilde{\beta}_T \cdot m_y, \tag{10}$$

with the anomalous $\tilde{\beta}_L$ coefficient value being far smaller than the conventional $\tilde{\beta}_T$ coefficient. To show the influence of $\tilde{\beta}_L$, it would be therefore necessary to access magnetization states with very small $m_y$ values or correspondingly very small $|\tilde{\beta}|$ values, which are, however, not accessible in our experiment. For the $|\tilde{\beta}|$ range that our experiments can cover, this anomalous dependence is not observed, and $\phi_{\tilde{\beta}}$ remains constant, as we see in Figs. 11(b) and 12(b).

## IV. CONCLUSIONS

In this paper, we have studied the accuracy of the reflection matrix description in linear MO. To accomplish this, we developed a suitable strategy for testing the **R** accuracy experimentally, and we designed and fabricated a suitable sample for accessing the most meaningful test conditions, which we managed to facilitate by means of a uniaxial magnetic sample with in-plane EA and macrospin behavior. Furthermore, we utilized GME as a characterization technique because it has the advantage of determining all the reflection matrix parameters in a single experiment with high precision. We found that, both for in-plane magnetization cases as well as for general magnetization cases that include an out-of-plane component, all test conditions were fulfilled to a very high degree of numerical precision. Thus, we were able to experimentally verify that the conventionally utilized reflection matrix description, given by Eq. (1), is indeed completely correct if the material under investigation fulfills the conditions under which Eq. (1) was derived. Those include that the pure optical response of the material is isotropic and that the MO coupling is isotropic as well. Furthermore, the derivation of Eq. (1) utilizes the fact that MO effects constitute a small perturbation of the optics so that considerations of linear MO terms are sufficient. Moreover, as GME enables the acquisition of quantitatively very precise results, we were also able to detect small deviations in our measurements from Eq. (1). They occur under specifically chosen experimental conditions and are related to the fact that Eq. (1) is not exactly applicable in our experiment, given that our sample exhibits weak MO anisotropy, which can in principle occur for any anisotropic magnetic sample. Once MO anisotropy is explicitly considered in the derivation of a reflection matrix analogous to Eq. (1), complete agreement between the modified matrix terms and our experimental data is reestablished.

## ACKNOWLEDGMENTS

This paper was supported by the Spanish Ministry of Science and Innovation under the Maria de Maeztu Units of Excellence Programme (Grant No. CEX2020-001038-M) and Project No. PID2021-123943NB-I00 (OPTOMETAMAG) as well as by Predoctoral Fellowship No. PRE2019-088428. C.M.V. acknowledges the Basque Government for Fellowship No. PRE_2022_2_0190.

[1] J. Kerr, On reflection of polarized light from the equatorial surface of a magnet, Philos. Mag. **5**, 161 (1878).

[2] J. Kerr, On rotation of the plane of polarization by reflection from the pole of a magnet, Philos. Mag. **3**, 321 (1877).

[3] P. Weinberger, John Kerr and his effects found in 1877 and 1878, Philos. Mag. Lett. **88**, 897 (2008).

[4] W. Rave, R. Schäfer, and A. Hubert, Quantitative observation of magnetic domains with the magneto-optical Kerr effect, J. Magn. Magn. Mater. **65**, 7 (1987).

[5] J. McCord, Progress in magnetic domain observation by advanced magneto-optical microscopy, J. Phys. D: Appl. Phys. **48**, 333001 (2015).

[6] I. V. Soldatov and R. Schäfer, Advances in quantitative Kerr microscopy, Phys. Rev. B **95**, 014426 (2017).

[7] A. Laraoui, M. Albrecht, and J.-Y. Bigot, Femtosecond magneto-optical Kerr microscopy, Opt. Lett. **32**, 936 (2007).

[8] O. Idigoras, P. Vavassori, J. M. Porro, and A. Berger, Kerr microscopy study of magnetization reversal in uniaxial Co-films, J. Magn. Magn. Mater. **322**, L57 (2010).

[9] K. Sato and T. Ishibashi, Fundamentals of magneto-optical spectroscopy, Front. Phys. **10**, 946515 (2022).

[10] I. Razdolski, A. Alekhin, U. Martens, D. Bürstel, D. Diesing, M. Münzenberg, U. Bovensiepen, and A. Melnikov, Analysis of the time-resolved magneto-optical Kerr effect for ultrafast magnetization dynamics in ferromagnetic thin films, J. Phys.: Condens. Matter **29**, 174002 (2017).

[11] A. Kimel, A. Zvezdin, S. Sharma, S. Shallcross, N. de Sousa, A. García-Martín, G. Salvan, J. Hamrle, O. Stejskal, J. McCord *et al.*, The 2022 magneto-optics roadmap, J. Phys. D: Appl. Phys. **55**, 463003 (2022).

[12] O. Idigoras, A. K. Suszka, P. Vavassori, B. Obry, B. Hillebrands, P. Landeros, and A. Berger, Magnetization reversal of in-plane uniaxial Co films and its dependence on epitaxial alignment, J. Appl. Phys. **115**, 083912 (2014).

[13] B. Van De Wiele, S. Fin, A. Sarella, P. Vavassori, and D. Bisero, How finite sample dimensions affect the reversal process of magnetic dot arrays, Appl. Phys. Lett. **105**, 162407 (2014).

[14] L. J. Heyderman, F. Nolting, D. Backes, S. Czekaj, L. Lopez-Diaz, M. Kläui, U. Rüdiger, C. A. F. Vaz, J. A. C. Bland, R. J. Matelon *et al.*, Magnetization reversal in cobalt antidot arrays, Phys. Rev. B **73**, 214429 (2006).

[15] E. R. Moog and S. D. Bader, Smoke signals from ferromagnetic monolayers: $p(1 \times 1)$ Fe/Au(100), Superlattices Microstruct. **1**, 543 (1985).

[16] A. Berger and M. R. Pufall, Quantitative vector magnetometry using generalized magneto-optical ellipsometry, J. Appl. Phys. **85**, 4583 (1999).

[17] K. Mok, N. Du, and H. Schmidt, Vector-magneto-optical generalized ellipsometry, Rev. Sci. Instrum. **82**, 033112 (2011).

[18] M. Vomir, L. H. F. Andrade, L. Guidoni, E. Beaurepaire, and J. Y. Bigot, Real Space Trajectory of the Ultrafast Magnetization Dynamics in Ferromagnetic Metals, Phys. Rev. Lett. **94**, 237601 (2005).

[19] L. H. F. Andrade, A. Laraoui, M. Vomir, D. Muller, J. P. Stoquert, C. Estournès, E. Beaurepaire, and J. Y. Bigot, Damped Precession of the Magnetization Vector of Superparamagnetic Nanoparticles Excited by Femtosecond Optical Pulses, Phys. Rev. Lett. **97**, 127401 (2006).

[20] A. Laraoui, J. Vénuat, V. Halté, M. Albrecht, E. Beaurepaire, and J. Y. Bigot, Study of individual ferromagnetic disks with femtosecond optical pulses, J. Appl. Phys. **101**, 09C105 (2007).

[21] C. M. Valderrama, M. Quintana, A. Martínez-De-Guerenu, T. Yamauchi, Y. Hamada, Y. Kurokawa, H. Yuasa, and A. Berger, Insertion layer magnetism detection and analysis using transverse magneto-optical Kerr effect (T-MOKE) ellipsometry, J. Phys. D. Appl. Phys. **54**, 435002 (2021).

[22] E. Oblak, P. Riego, L. Fallarino, A. Martínez-De-Guerenu, F. Arizti, and A. Berger, Ultrasensitive transverse magneto-optical

Kerr effect measurements by means of effective polarization change detection, J. Phys. D. Appl. Phys. **50**, 23LT01 (2017).
[23] G. Armelles, A. Cebollada, A. García-Martín, and M. U. González, Magnetoplasmonics: Combining magnetic and plasmonic functionalities, Adv. Opt. Mater. **1**, 10 (2013).
[24] C. Stamm, C. Murer, M. Berritta, J. Feng, M. Gabureac, P. M. Oppeneer, and P. Gambardella, Magneto-Optical Detection of the Spin Hall Effect in Pt and W Thin Films, Phys. Rev. Lett. **119**, 087203 (2017).
[25] J. Puebla, F. Auvray, M. Xu, B. Rana, A. Albouy, H. Tsai, K. Kondou, G. Tatara, and Y. Otani, Direct optical observation of spin accumulation at nonmagnetic metal/oxide interface, Appl. Phys. Lett. **111**, 092402 (2017).
[26] E. Jiménez, N. Mikuszeit, J. L. F. Cuñado, P. Perna, J. Pedrosa, D. Maccariello, C. Rodrigo, M. A. Niño, A. Bollero, J. Camarero *et al.*, Vectorial Kerr magnetometer for simultaneous and quantitative measurements of the in-plane magnetization components, Rev. Sci. Instrum. **85**, 053904 (2014).
[27] J. B. González-Díaz, J. A. Arregi, A. Martínez-De-Guerenu, F. Arizti, and A. Berger, Quantitative magneto-optical characterization of diffusive reflected light from rough steel samples, J. Appl. Phys. **113**, 153904 (2013).
[28] C. Daboo, J. A. C. Bland, R. J. Hicken, A. J. R. Ives, M. J. Baird, and M. J. Walker, Vectorial magnetometry with the magneto-optic Kerr effect applied to Co/Cu/Co trilayer structures, Phys. Rev. B **47**, 11852 (1993).
[29] A. Berger and M. R. Pufall, Generalized magneto-optical ellipsometry, Appl. Phys. Lett. **71**, 965 (1997).
[30] E. Oblak, P. Riego, A. Garcia-Manso, A. Martínez-De-Guerenu, F. Arizti, I. Artetxe, and A. Berger, Ultrasensitive transverse magneto-optical Kerr effect measurements using an effective ellipsometric detection scheme, J. Phys. D: Appl. Phys. **53**, 205001 (2020).
[31] C. M. Valderrama, M. Quintana, A. Martínez-de-Guerenu, T. Yamauchi, Y. Hamada, Y. Kurokawa, H. Yuasa, and A. Berger, Sensitivity and reproducibility of transverse magneto-optical Kerr effect (T-MOKE) ellipsometry, J. Phys. D. Appl. Phys. **55**, 435007 (2022).
[32] J. M. Florczak and E. D. Dahlberg, Detecting two magnetization components by the magneto-optical Kerr effect, J. Appl. Phys. **67**, 7520 (1990).
[33] S. Polisetty, J. Scheffler, S. Sahoo, Y. Wang, T. Mukherjee, X. He, and C. Binek, Optimization of magneto-optical Kerr setup: Analyzing experimental assemblies using Jones matrix formalism, Rev. Sci. Instrum. **79**, 055107 (2008).
[34] C.-Y. You and S.-C. Shin, Generalized analytic formulae for magneto-optical Kerr effects, J. Appl. Phys. **84**, 541 (1998).
[35] Š. Višňovský, Magneto-optical ellipsometry, Czech. J. Phys. **36**, 625 (1986).
[36] M. Schubert, Polarization-dependent optical parameters of arbitrarily anisotropic homogeneous layered systems, Phys. Rev. B **53**, 4265 (1996).
[37] J. Zak, E. R. Moog, C. Liu, and S. D. Bader, Universal approach to magneto-optics, J. Magn. Magn. Mater. **89**, 107 (1990).
[38] M. Schubert, T. E. Tiwald, and J. A. Woollam, Explicit solutions for the optical properties of arbitrary magneto-optic materials in generalized ellipsometry, Appl. Opt. **38**, 177 (1999).
[39] T. Higo, H. Man, D. B. Gopman, L. Wu, T. Koretsune, O. M. J. van 't Erve, Y. P. Kabanov, D. Rees, Y. Li, M.-T. Suzuki *et al.*, Large magneto-optical Kerr effect and imaging of magnetic octupole domains in an antiferromagnetic metal, Nat. Photonics **12**, 73 (2018).
[40] F. M. Bartram, S. Sorn, Z. Li, K. Hwangbo, S. Shen, F. Frontini, L. He, P. Yu, A. Paramekanti, and L. Yang, Anomalous Kerr effect in $SrRuO_3$ thin films, Phys. Rev. B **102**, 140408(R) (2020).
[41] T. Uchimura, J.-Y. Yoon, Y. Sato, Y. Takeuchi, S. Kanai, R. Takechi, K. Kishi, Y. Yamane, S. DuttaGupta, J. Ieda *et al.*, Observation of domain structure in non-collinear antiferromagnetic $Mn_3Sn$ thin films by magneto-optical Kerr effect, Appl. Phys. Lett. **120**, 172405 (2022).
[42] P. Riego, L. Fallarino, C. Martínez-Oliver, and A. Berger, Magnetic anisotropy of uniaxial ferromagnets near the Curie temperature, Phys. Rev. B **102**, 174436 (2020).
[43] D. Weller, H. Brändle, G. Gorman, C. J. Lin, and H. Notarys, Magnetic and magneto-optical properties of cobalt-platinum alloys with perpendicular magnetic anisotropy, Appl. Phys. Lett. **61**, 2726 (1992).
[44] W. Yang, D. N. Lambeth, and D. E. Laughlin, Unicrystal Co–alloy media on Si(110), J. Appl. Phys. **85**, 4723 (1999).
[45] O. Idigoras, U. Palomares, A. K. Suszka, L. Fallarino, and A. Berger, Magnetic properties of room temperature grown epitaxial $Co_{1-x}Ru_x$−alloy films, Appl. Phys. Lett. **103**, 102410 (2013).
[46] L. Fallarino, B. J. Kirby, M. Pancaldi, P. Riego, A. L. Balk, C. W. Miller, P. Vavassori, and A. Berger, Magnetic properties of epitaxial CoCr films with depth-dependent exchange-coupling profiles, Phys. Rev. B **95**, 134445 (2017).
[47] L. Fallarino, P. Riego, B. J. Kirby, C. W. Miller, and A. Berger, Modulation of magnetic properties at the nanometer scale in continuously graded ferromagnets, Materials (Basel). **11**, 251 (2018).
[48] M. Quintana, A. Meléndez, C. M. Valderrama, L. Fallarino, and A. Berger, Temperature-Independent Coercivity in Compositionally Graded Ferromagnetic Multilayers, Phys. Rev. Appl. **18**, 054024 (2022).
[49] E. C. Stoner and E. P. Wohlfarth, A mechanism of magnetic hysteresis in heterogeneous alloys, Philos. Trans. R. Soc. A **240**, 599 (1948).
[50] M. Grimsditch, E. E. Fullerton, and R. L. Stamps, Exchange and anisotropy effects on spin waves in epitaxial Co films, Phys. Rev. B **56**, 2617 (1997).
[51] P. Riego, Magneto-optical characterization of magnetic thin films and interface structures, Ph.D. thesis, Universidad del País Vasco, 2019.
[52] J. A. Arregi, J. B. Gonzalez-Diaz, E. Bergaretxe, O. Idigoras, T. Unsal, and A. Berger, Study of generalized magneto-optical ellipsometry measurement reliability, J. Appl. Phys. **111**, 103912 (2012).
[53] J. Ander, Magneto-optical ellipsometry and magnetometry of thin films and multilayers, Ph.D. thesis, Universidad del País Vasco, 2020.
[54] J. B. González-Díaz, J. A. Arregi, E. Bergaretxe, M. J. Fertin, O. Idigoras, and A. Berger, Anomalous magneto-optical behavior of uniaxial Co/CoO bilayer films, J. Magn. Magn. Mater. **325**, 147 (2013).
[55] J. A. Arregi, P. Riego, and A. Berger, What is the longitudinal magneto-optical Kerr effect? J. Phys. D. Appl. Phys. **50**, 03LT01 (2017).